City Research Online

City, University of London Institutional Repository

This is the accepted version of the paper.

This version of the publication may differ from the final published version.

Permanent repository link: http://openaccess.city.ac.uk/15678/

Link to published version: http://dx.doi.org/10.1016/j.fuel.2016.08.014

City Research Online: http://openaccess.city.ac.uk/   publications@city.ac.uk

1   **Aerodynamic breakup of an n-decane droplet in a high temperature**

2   **gas environment**

3

4   George Strotos[1,a,*], Ilias Malgarinos[1,b], Nikos Nikolopoulos[1,c], Manolis Gavaises[1,d]

5   [1]School of Engineering and Mathematical Sciences, City University London, Northampton

6   Square, EC1V 0HB, London, UK

7   [a] George.Strotos.1@city.ac.uk

8   [b] Ilias.Malgarinos.1@city.ac.uk

9   [c] Nikolaos.Nikolopoulos.1@city.ac.uk

10   [d] M.Gavaises@city.ac.uk

11   [*]Corresponding author

12

13   **Abstract**

14   The aerodynamic droplet breakup under the influence of heating and evaporation is studied

15   numerically by solving the Navier-Stokes, energy and transport of species conservation

16   equations; the VOF methodology is utilized in order to capture the liquid-air interphase. The

17   conditions examined refer to an n-decane droplet with Weber numbers in the range 15-90 and

18   gas phase temperatures in the range 600-1000K at atmospheric pressure. To assess the effect

19   of heating, the same cases are also examined under isothermal conditions and assuming

20   constant physical properties of the liquid and surrounding air. Under non-isothermal

21   conditions, the surface tension coefficient decreases due to the droplet heat-up and promotes

22   breakup. This is more evident for the cases of lower Weber number and higher gas phase

temperature. The present results are also compared against previously published ones for a more volatile n-heptane droplet and reveal that fuels with a lower volatility are more prone to breakup. A 0-D model accounting for the temporal variation of the heat/mass transfer numbers is proposed, able to predict with sufficient accuracy the thermal behavior of the deformed droplet.

Keywords: droplet breakup; VOF; heating; evaporation

1   Introduction

The efficiency of spray combustion systems is determined by the dispersion of the spray droplets which increase the surface area and subsequently the rates of heat and mass transfer. Following the primary jet breakup, the produced droplets are subjected to secondary breakup which further enhances the heat/mass transfer rates. The coupled problem of secondary droplet breakup under the influence of heating and evaporation is of major engineering interest, but due to its complexity has not been yet addressed in detail and the vast majority of relevant works examine these two phenomena independently.

Droplets under the influence of aerodynamic forces are subjected to different breakup modes, namely the bag breakup, the transitional breakup, the sheet-thinning breakup and the catastrophic breakup; for details see Guildenbecher et al. [1] among many others. The outcome of the breakup is determined by the relative strength of the aerodynamic, surface tension, viscous and external body forces acting on the droplet. These are grouped into dimensionless numbers, forming the Weber number (We), the Reynolds number (Re), the Ohnesorge number (Oh), the density ratio (ε) and the viscosity ratio (N), as shown in Eq. 1, while under certain flow conditions other parameters such as the Froude number, the Mach number and the turbulence levels may become important.

2

$$We = \frac{\rho_g U_{rel,0}^2 D_0}{\sigma} \quad Re = \frac{\rho_g U_{rel,0} D_0}{\mu_g} \quad Oh = \frac{\mu_l}{\sqrt{\rho_l \sigma D_0}} \quad \varepsilon = \frac{\rho_l}{\rho_g} \quad N = \frac{\mu_l}{\mu_g} \qquad (1)$$

47

48   The phenomena observed during droplet breakup have been addressed in review studies such

49   as those of [1-5] among others; it is generally considered that the *We* number is the most

50   influential parameter, while viscous effects become important when *Oh*>0.1. The breakup

51   process requires some finite time to be established and the duration of the phenomenon is in

52   the order of the shear breakup timescale t_{sh} proposed by Nicholls and Ranger [6]:

$$t_{sh} = \frac{D_0}{U_{rel,0}} \sqrt{\varepsilon} \qquad (2)$$

53

54   Many works have studied either experimentally or numerically the droplet breakup, aiming to

55   enlighten the conditions leading to the different breakup regimes and the underlying physics.

56   Selective experimental studies on droplet breakup are those of [7-22] but generally, there is a

57   scattering of the experimental findings which is probably due to the variety of the

58   experimental techniques used and the experimental uncertainties. Numerical works aiming to

59   fill the gap in knowledge such as those of [23-32]; they have examined the isothermal droplet

60   breakup in 2-D and 3-D computational domains and they have provided useful information

61   into the detailed processes inside and in the vicinity of the droplets during droplet breakup,

62   which are difficult to be determined with experimental techniques. More specifically, [7-10]

63   provided breakup maps in the *We-Oh* plane, [11-13, 16] further clarified the boundaries

64   between different breakup regimes, [14, 15, 20, 23, 25, 30, 31] clarified the physical

65   mechanisms behind the breakup regimes, [13, 18] examined the size distribution of the child

66   droplets after the parent droplet disintegration, [22] identified experimentally the gas flow

67   structure during droplet breakup, [15, 24, 26, 32] examined the effect of density ratio and [26,

68   27, 29, 31] examined the droplet drag coefficient. For a detailed presentation of the works

69   referring to droplet breakup, see Strotos et al. [33].

70   Regarding the evaporation studies, in addition to 0-D or 1-D models (see details in the review

71   articles of [34-37] among others), detailed CFD works solving the complete Navier-Stokes

72   and heat/mass transfer equations have also been published. Selectively, the works of [38-47]

73   refer to single component evaporation and [48-53] refer to multicomponent droplet

74   evaporation, providing detailed information in the transport processes between the liquid and

75   the gas phase. More specifically, [39, 40] were the first who solved the complete set of the

76   governing equations, [42, 47] modelled the presence of the suspender, [43] examined the

77   effect of thermocapillary flow,   [44] studied the effect of turbulence and [46] proposed

78   numerical improvements for the evaporation modelling. Similarly, in multicomponent studies

79   the first ones were those of [48, 49], followed by [50] who included variable thermophysical

80   properties and [52, 53] which conducted parametric studies. The aforementioned studies were

81   restricted to the modelling of isolated spherical droplets and a detailed presentation of the

82   works referring to droplet evaporation, was given in Strotos et al. [54].

83   Regarding the coupled problem of droplet breakup and evaporation, this has not yet been

84   studied in detail except in the CFD works of [55-60]. Haywood et al. [55, 56] showed that for

85   droplets under steady or unsteady (oscillatory) deformation, the quasi-steady correlations for

86   Nusselt (*Nu*) and Sherwood (*Sh*) numbers are still valid when a volume-equivalent diameter is

87   used, Mao et al. [57] showed that the mass transfer from deformed droplets is mainly

88   controlled by the Peclet (*Pe*) number, while the *We* number has a small impact only at high

89   *Pe* numbers. Hase and Weigand [58] studied the effect of droplet deformation on the heat

90   transfer enhancement and they found that this increases due to the oscillatory droplet motion

91   and the increased surface area of the deformed droplets; moreover, the steady-state classical

92   correlations for the *Nu* number, under-predict the heat transfer at the beginning of the

93   simulation. Later, Schlottke et al. [59] included the evaporation in their model and they found

94   that the droplet heating is affected by the flow field inside the droplet which transfers hotter

95   fluid from the droplet surface towards inside. Cerqueira et al. [60] studied spherical and

96   deformed rising bubbles and proposed new correlations for the *Nu* and *Sh* numbers.

97   The aforementioned studies were restricted to *We* number below 10, which limits the results

98   to small droplet deformation without breakup. Recently, Strotos et al. [61] examined the

99   effect of heating and evaporation in cases undergoing breakup for *We*=15-90. They examined

100   volatile n-heptane droplets and they showed that the droplet heating becomes increasingly

101   influential during breakup for lower *We* number and higher gas temperature. The present

102   numerical work is a continuation of this work and examines an n-decane droplet with

103   substantially lower volatility than the n-heptane; this promotes the higher heating of the

104   droplet. This work is the first examining the combined effect of heating and breakup solving

105   the Navier-Stokes, energy and transport of species equations coupled with interface capturing,

106   for a wide range of We numbers, gas phase temperatures for this particular fuel while it

107   compares it with the less volatile one for similar flow conditions. The structure of the paper

108   includes a brief description of the numerical model and the cases examined, followed by the

109   results, while the most important conclusions are summarized at the end.

110

2   Numerical model and methodology

112   The continuous field representation of the two-phase flow with the VOF methodology is used

113   to study the droplet breakup. The problem is assumed to be 2-D axisymmetric and an

114   automatic local grid refinement technique [62, 63] enhances the accuracy of the computations

115   at the interface region, while achieving low computational cost compared to a simulation with

116   a uniform grid of the same density. The droplet heating and evaporation are accounted for by

117   solving the energy and vapor transport equations, while the local evaporation rate is obtained

118   by using a model based on Fick's law, which is independent of the droplet shape. The species

5

119   properties depend on the local temperature [64, 65] and mass averaging rules are used for the

120   gaseous mixture assuming incompressible ideal gas. For the complete presentation of the

121   equations solved, the reader is referred to Strotos et al. [54]. The simulations were performed

122   with the commercial CFD tool ANSYS FLUENT v14.5 [66] and the numerical settings

123   adopted as also the User Defined Functions (UDFs) are identical to those used in Strotos et al.

124   [61].

125   The model has been successfully validated in [33, 54, 63, 67, 68] for cases including the

126   motion of a free falling droplet, droplet breakup, droplet evaporation and droplet impact onto

127   a solid substrate.

128

3   Results and discussion

3.1   Cases examined and numerical setup

131   The cases examined are similar to those presented in Strotos et al. [61] for a volatile n-

132   heptane droplet (C07), but this time an n-decane (C10) droplet is examined which has a much

133   lower volatility (i.e. vapor pressure) than the n-heptane. The cases examined refer to a small

134   100μm diameter droplet with an initial temperature of T_0=300K, corresponding to Oh=0.02

135   which is low enough to guarantee breakup process almost independent from the Oh number.

136   The droplet is assumed to be initially motionless and it is subjected to a step change of the gas

137   phase velocity leading to We numbers in the range 15-90. The ambient air has a high

138   temperature in the range 600-1000K ($T_{cr,C10}$=617.7K) which correspond to high density and

139   viscosity ratios (ε>1200 and N>20 respectively) and thus the breakup outcome is not affected

140   by them since ε>32 [24]. The aforementioned combination of We numbers and gas phase

141   temperatures corresponds to gas phase velocities in the range 77-243m/s; these in turn

142   correspond to Re numbers in the range 84-367 which ensures that the flow remains laminar

6

143 and axisymmetric [69, 70]; the Mach numbers are below 0.38, which implies that the

144 compressibility effects can be ignored. For all cases examined, the ambient pressure is

145 atmospheric; thus no modifications capturing high pressure effects are required in the

146 evaporation model. A graphical representation of the cases examined is shown in Fig. 1 on the

147 *We-Re* map. These cases were examined both for evaporating and isothermal conditions. For

148 the latter, the energy equation and the evaporation source terms were not accounted for, while

149 the species properties were kept constant at their reference temperature values, i.e. at

150 T_0=300K for the liquid droplet and at T_∞ for the surrounding air; the isothermal runs

151 correspond to a parametric study for the effect of *We* and *Re* numbers.

152
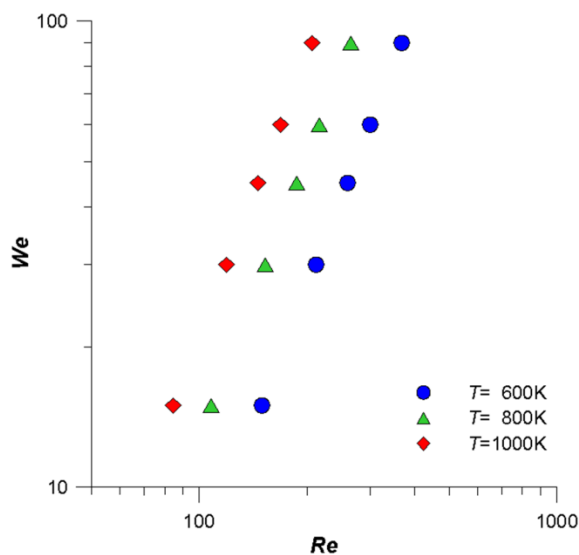
153

154 Fig. 1: Cases examined on the *We-Re* plane.

155

156 Regarding the computational domain and the boundary conditions, these are the same as in

157 Strotos et al. [33, 61, 68], in which a step change of the gas phase velocity is applied around

158 the initially motionless droplet; the 2-D axisymmetric computational domain is moving with

159 the average translational droplet velocity. Upwind the droplet, Dirichlet boundary conditions

160   were applied (i.e. fixed velocity and temperature for the non-isothermal cases) and downwind

161   Neumann boundary conditions (i.e. zero first gradient for all variables) were used. A locally

162   refined grid with 192 cells per radius was used, able to resolve the boundary layers at the

163   interface region as explained in Strotos et al. [61]. It has to be noted that the 2D simulations

164   performed in this work are considered reliable up to the breakup instant, since after that,

165   three-dimensional phenomena appear.

166   In an effort to relate and also distinguish the simulations performed in Strotos et al. [61] for

167   the volatile n-heptane droplet, from the present simulations referring to n-decane, the heat and

168   mass transfer Spalding numbers (B_T and B_M respectively) are considered (Eqs. 3 and 4). These

169   are calculated by using the initial surface temperature $T_{s,0}$ (Eq. 5) which corresponds to the

170   contact temperature between semi-infinite solids [71]; this concept was also used in [72-74]

171   for droplet impact on hot substrates and agrees well with the CFD predictions at the first time-

172   step.

$$B_{T,\infty} = \frac{c_{p,g,\infty}(T_\infty - T_0)}{L(T_{s,0})} \tag{3}$$

$$B_{M,0} = \frac{Y_s(T_{s,0}) - Y_\infty}{1 - Y_s(T_{s,0})} \tag{4}$$

$$T_{s,0} = \frac{\gamma_l T_0 + \gamma_g T_\infty}{\gamma_l + \gamma_g} \tag{5}$$

$$F_{heat} = \frac{1 + B_{T,\infty}}{1 + B_{M,0}} \tag{6}$$

173   The droplet's tendency to increase its temperature is proportional to B_T and inversely

174   proportional to B_M, since the evaporation absorbs heat and tends to decrease the droplet

175   temperature. An indicator of the droplet heat-up is the heating factor F_{heat} (Eq. 6); large values

176   imply a high tendency to increase the temperature. A comparison of the heating factor for the

177   n-heptane (C07) and the n-decane (C10) is shown in Fig. 2 as a function of the gas phase

178   temperature for T_0=300K (note that this is independent of the flow conditions). It is evident

179   that the n-decane has a higher possibility to heat-up due to its lower vapor pressure; the

180   heating factor increases with the gas phase temperature and decreases with increasing initial

181   fuel temperature (not shown in Fig. 2). It has to be noted that the heating factor has a

182   qualitative character and for the isothermal cases it was assumed that F_{heat}=1, which

183   corresponds to infinite latent heat and zero vapor pressure. Note that the definition of the

184   heating factor adopted here is suitable for the present conditions, but might not be suitable for

185   low ambient temperatures close to the droplet temperature in which F_{heat}<1.

186
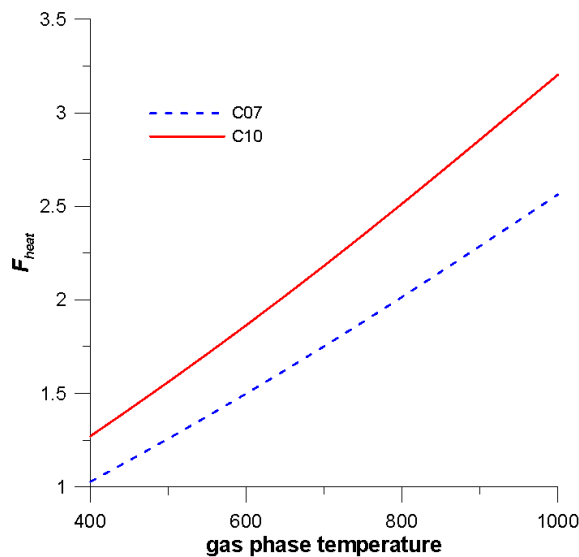
188   Fig. 2: Heating factor as a function of the gas phase temperature for two different fuels

189   (T_0=300K).

190

191   Finally, prior to the presentation of the results of the present work, it has to be noted that the

192   isothermal simulations conducted in Strotos et al. [61] for an n-heptane and the present

193   simulations for an n-decane are in close agreement between them since they both have low

194   *Oh* numbers (0.01 and 0.02 respectively) and similar *Re* number ranges (77-337 and 84-367

9

195 respectively for T_∞=600-1000K). On the other hand, the evaporating simulations for these two

196 fuels are exhibiting large variations due to the species thermal properties.

197

3.2 Hydrodynamic effect of heating

199 The results obtained for the droplet shapes are shown in Fig. 3 and Fig. 4 for the cases with

200 free stream temperature 800 and 1000K respectively. In these figures the left part corresponds

201 to the isothermal predictions and the right part to the evaporating simulations; the cases with

202 T_∞=600K are not presented since the differences between isothermal and evaporating

203 simulations were small. The droplet shapes drawn in black correspond to time intervals of

204 $0.5t_{sh}$ (i.e. 0.0, 0.5, 1.0, 1.5, 2.0t_{sh}) and the droplet shapes drawn in red correspond to

205 intermediate instances i.e. 0.75, 1.25, 1.75, 2.25t_{sh} (the time instant of $0.25t_{sh}$ has been

206 omitted); the last droplet shape corresponds to the instant of breakup. From figures Fig. 3 and

207 Fig. 4 it is evident that the We number is the most influential parameter leading to different

208 breakup regimes as the We number increases, namely the bag breakup for low We numbers,

209 the transitional breakup for intermediate We numbers and the sheet-thinning breakup for the

210 highest We number examined. Nevertheless, the sheet-thinning breakup is not clear due to the

211 low Re number and the continuous transition between the different breakup regimes; the

212 effect of Re number and the existence of a critical Re number leading to bag breakup at

213 We=15 was in detail discussed in Strotos et al. [61] and similar comments were also made in

214 Han and Tryggvason [23] and Guildenbecher et al. [1].

215 Apart from the dominant role of We number, the droplet heating is playing an important role

216 for the low We number cases. Under isothermal conditions, droplets with We=15 and

217 T_∞>800K are not breaking up due to the low Re number. At the same We number when

218 heating is accounted for with T_∞=800K (Fig. 3), a clear bag breakup is predicted; this is even

219 more emphatic for the case of T_∞=1000K (Fig. 4) in which the droplet not only breaks up, but

10

220   the breakup regime predicted is the transitional breakup. To the authors best knowledge, no

221   previous study has reported transitional break-up at such a low *We* number; this is purely due

222   to the droplet heating which reduces the surface tension coefficient and subsequently the

223   forces tending to resist the droplet deformation. Note that the effect of heating was not so

224   profound in the high volatility n-heptane examined in Strotos et al. [61].

225
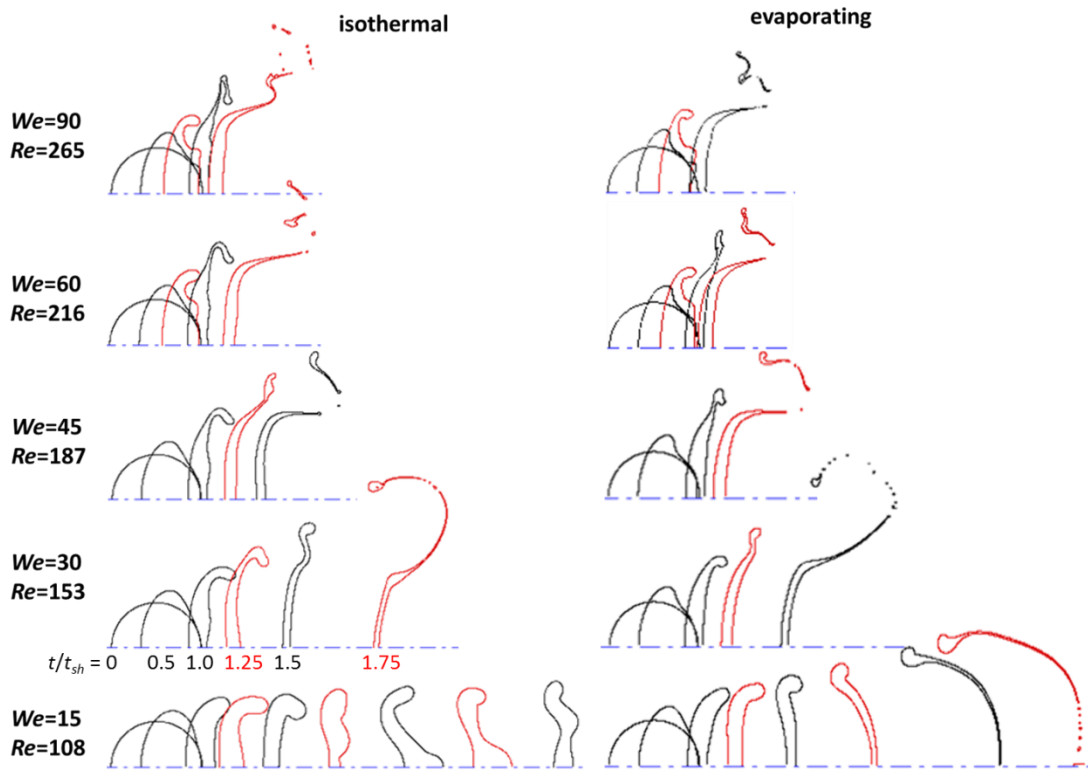
226

227   Fig. 3: Droplet shape evolution for the cases with T_∞=800K. The droplet shapes drawn black

228   (see the online version) correspond to time intervals of $0.5t_{sh}$ and the droplet shapes drawn red

229   correspond to representative intermediate instances of $0.25t_{sh}$. The last droplet shape

230   corresponds to the instant of breakup. Differences are observed at the lower *We* number case.

231
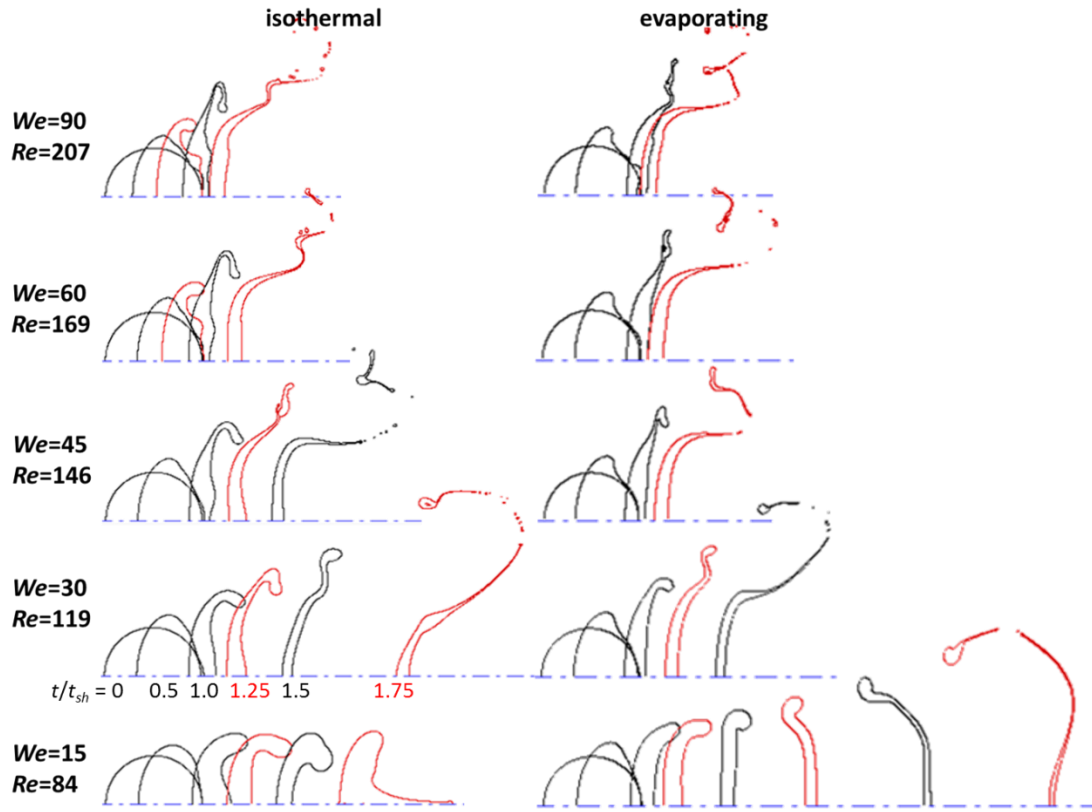
Fig. 4: Droplet shapes for the cases with $T_\infty=1000K$. The droplet shapes drawn black (see the online version) correspond to time intervals of $0.5t_{sh}$ and the drawn red correspond to representative intermediate instances of $0.25t_{sh}$. The last droplet shape corresponds to the instant of breakup. Differences are observed at the lower We number case.

The predicted onset of breakup t_{br} (termed also as "initiation time") for all cases examined is shown in Fig. 5, along with the corresponding experimental correlations given by Pilch and Erdman [2] and Dai and Faeth [13], abbreviated as "P-E 1987" and "D-F 2001" respectively; the present data for the breakup time are subjected to error of the order of $0.05t_{sh}$ (2.5-5%) due to the estimation of the breakup time by examining post-processed images. The experimental correlations differ between them due to several experimental uncertainties [25]. The trends are correctly captured by predicting faster breakup with increasing We number. The isothermal cases exhibit a weak dependency on Re number when the We is kept constant,

246   while in the evaporating cases the reduction of the surface tension coefficient acts as if the *We*

247   number was higher; subsequently the droplet breaks up is faster. A best fit curve of the

248   breakup time for both evaporating and isothermal cases is given in Eq. 7 valid for the entire

249   range of conditions examined, i.e n-decane fuel, *Oh*=0.02, *We*=15-90, *Re*=84-367 and

250   *T*$_\infty$=600-1000K.

$$t_{br}/t_{sh} = 8.628 We^{-0.352} Re^{-0.086} F_{heat}^{-0.116} \tag{7}$$

251
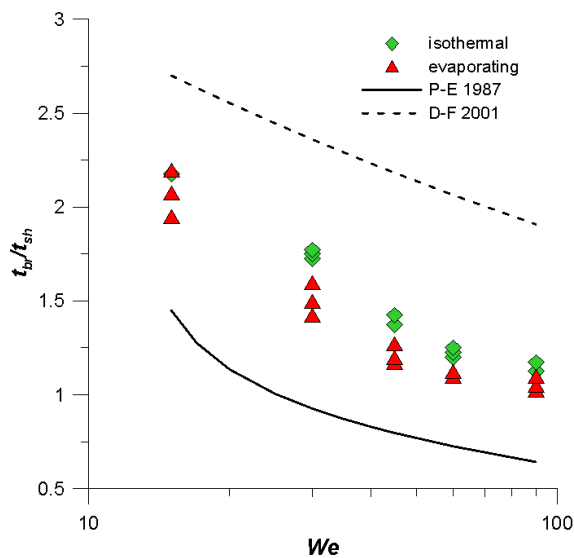
253   Fig. 5: Predicted dimensionless breakup time for the isothermal and the evaporating n-decane

254   cases.

255

256   One of the most important magnitudes determining the combustion efficiency is the droplet

257   surface area (*S*) which deviates significantly from the corresponding of the initial spherical

258   shape (*S$_0$*) during the droplet deformation and breakup and it is difficult to be measured

259   experimentally. The temporal evolution of this quantity is presented in Fig. 6 for selected

260   cases (*T*$_\infty$=800K and *We*=15, 30, 90); note that for the isothermal case with *We*=15, the

13

261 droplet is not breaking up. In all cases, after an initial non-deforming period of $\sim 0.3t_{sh}$, the

262 droplet surface area starts to increase with a fast rate (1.6-5.7 in terms of non-dimensional

263 units) proportional to the *We* number, which is in accordance with the findings of Han and

264 Tryggvason [23]. Up to $t=t_{sh}$ the variation of the surface area is smooth, but at subsequent

265 times the rate of deformation may change due to surface instabilities appearing even in the

266 isothermal cases. For that reason, the maximum surface area at the instant of breakup is not

267 following a smooth variation as the *We* number is changing and a local maximum is observed

268 at *We*=30 (as it was also shown in [61]) reaching values of $12S_0$. This point needs further

269 investigation by performing 3-D simulations since 3-D phenomena may appear before the

270 breakup instant and alter both the rate of deformation as also the breakup instant. Regarding

271 the effect of heating (see the solid lines in Fig. 6), it is evident that it is important for low to

272 medium *We* numbers and $t>t_{sh}$ by further increasing the rate of deformation.

273
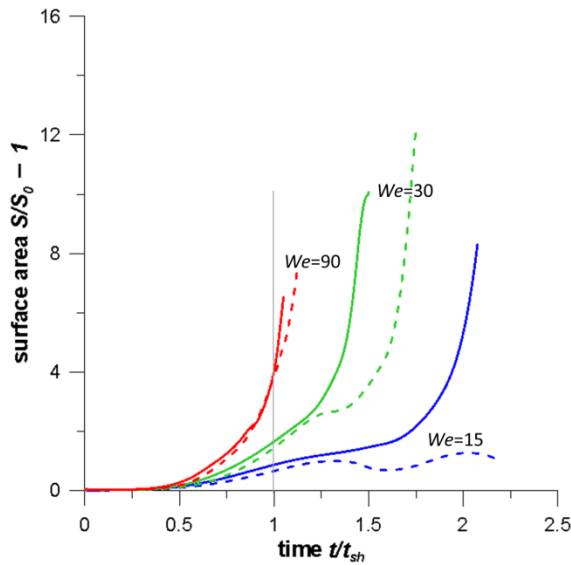
274

275 Fig. 6: Temporal evolution of the dimensionless droplet surface area for selected cases with

276 T_∞=800K. The dashed lines correspond to the isothermal cases and the solid lines to the

277 evaporating cases.

14

278

279   As explained in Strotos et al. [61] it is difficult to find a mathematical expression predicting

280   the temporal evolution of the surface area for the entire phenomenon up to the breakup instant

281   and covering the entire range of *We* numbers leading to different breakup regimes. This

282   becomes even more complex when heating is included since the surface area evolution is

283   implicitly coupled with the variation of the surface tension coefficient due to heating. On the

284   other hand, the evolution of the surface area can be predicted for $t<t_{sh}$ with Eq. 8a, which has

285   been slightly modified relative to the one used in [61] by using in the denominator on the

286   right hand side of Eq. 8a the term *sinh(c₂)*. Now, the coefficient c_1 expresses the surface area

287   at $t=t_{sh}$ and c_2 characterizes the form of the curve connecting the initial and the "final" state at

288    $t=0$ and $t=t_{sh}$ respectively; a low c_2 value implies a smoother (closer to the linear) variation.

289   An important improvement of the present fitting curve relative to the one in [61], is the

290   inclusion of the effect of heating by using the correction factor f_{corr} in the adjustable

291   coefficients c_1 and c_2 (see Eqs. 8b and c). Eq. 8 is valid for the entire range of conditions

292   examined in the present work, the correlation coefficient for the fitting of the surface area

293   evolution is above 0.98 and the prediction of the surface area at $t=t_{sh}$ is within the 15% error

294   for most of the cases examined; nevertheless this can reach values of 30% for specific cases at

295   the highest temperature of 1000K.

296

$$\frac{S}{S_0} - 1 = c_1 \frac{sinh(c_2 \cdot t/t_{sh})}{sinh(c_2)}, \qquad t < t_{sh} \tag{8a}$$

$$c_1 = 0.1484 We^{1.092} Re^{-0.284} f_{corr}, \quad f_{corr} = 1 + 4.152 We^{-1.06} (F_{heat} - 1)^{0.84} \tag{8b}$$

$$c_2 = 4.5234 We^{0.294} Re^{-0.198} f_{corr}, \quad f_{corr} = 1 - 0.013 We^{-0.50} (F_{heat} - 1)^{0.289} \tag{8c}$$

297

15

298   For the isothermal cases (f_{corr}=1) the surface area increases with increasing We number and

299   decreasing Re number; this is clearly derived from the sign of the exponents of c_1 (Eq. 8b).

300   When heating is included, the phenomenon becomes more complicated and the correction

301   factor f_{corr} depends both on the We number and the heating factor F_{heat}. The correction factor

302   for the coefficient c_1 is always f_{corr}>1 which means that heating tends to increase the surface

303   area at t=t_{sh}. As stated in [61], the extrapolation of this curve up to t_{br} should be done with

304   caution and limit the maximum value not to exceed 10-12S_0, otherwise unphysical values may

305   be obtained.

306   The droplet breakup is governed by the relative strength of the forces acting on the droplet,

307   which vary dynamically as the droplet shape, dimensions and velocity change during the

308   whole process. The instantaneous deforming forces scale with $\rho_g u_{rel,t}^2 D_{c,t}^2$ where $u_{rel,t}$ is the

309   instantaneous relative drop-gas velocity (obtained by subtracting the average droplet velocity

310   from the free-stream velocity) and $D_{c,t}$ is the instantaneous cross-stream diameter, while the

311   instantaneous restorative forces scale with $\sigma D_{c,t}$ in which the viscous forces have been ignored

312   since Oh<0.1. The ratio of these forces represents an instantaneous We number (see Eq. 9)

313   which changes during the breakup process and includes the effects of heating, deformation

314   and velocity change:

$$We_t = \frac{\rho_g u_{rel,t}^2 D_{c,t}}{\sigma} = We_0 \left(\frac{\sigma_0}{\sigma}\right)\left(\frac{D_{c,t}}{D_0}\right)\left(\frac{u_{rel,t}}{U_0}\right)^2 \tag{9}$$

315   The predicted transient We number based on Eq. 9 is plotted in Fig. 7 for selected isothermal

316   and evaporating cases with T_∞=800K. The transient We number increases in time implying

317   that the deforming forces become progressively stronger, except of the isothermal case with

318   We=15. In this case the droplet is not breaking up and after reaching a maximum, the

319   instantaneous We number decreases, implying that the restorative forces become stronger.

320   Generally, the instantaneous We number (as defined in Eq. 9) increases by a factor of 2-3

321   relative to the initial We number which is mainly ought to the increase of the cross sectional

diameter; the reduction of the relative drop-gas velocity (no more than 10% for the cases

examined) and the reduction of the surface tension coefficient play a secondary role. In Fig. 7

324 the curves derived from Eq. 9 by using either the experimental breakup time of Dai and Faeth

325 [13] or that of Pilch and Erdman [2] for Oh=0.02 are also shown; these were derived by

326 processing the experimental data of [13] and more details can be found in [61]. These curves

327 represent the critical instantaneous condition for breakup and when crossed, breakup occurs.

328 The present simulations qualitatively agree with these curves.

329
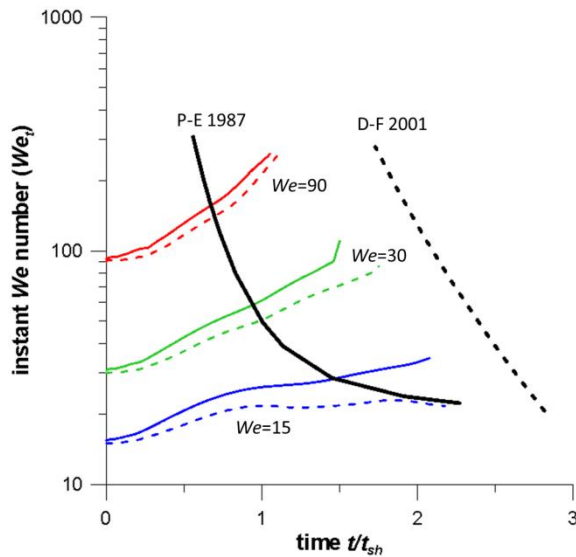
330

331 Fig. 7: Predicted instant We number for selected isothermal (dashed lines) and evaporating

332 (solid lines) cases with T_∞=800K.

333

3.3 Thermal behavior of the droplet

335 The temporal evolution of the mean volume averaged droplet temperature T_m and the spatially

336 averaged surface temperature T_s are shown in Fig. 8a with the solid and dashed lines

337 respectively, for two cases combining different We numbers and gas phase temperatures;

17

338   these are indicated inside the parentheses as (We,T_∞). Both the mean droplet temperature and

339   the surface temperature increase with increasing ambient temperature, as expected. The mean

340   droplet temperature T_m increases continuously in time and may reach a heat-up of 15K by the

341   onset of breakup, while the average surface temperature T_s exhibits a quite transient behavior;

342   during the flattening phase ($t<0.6$-$0.8t_{sh}$) the surface temperature increases until reaching a

343   maximum, followed by a decrease until coming closer to the volume averaged temperature.

344   This behavior is mainly attributed to the flow patterns induced by the shape distortion which

345   exchange hotter fluid from the droplet surface with the colder fluid from the droplet interior

346   (see also Schlottke et al [59]). Additional to that, the increased surface temperature results in a

347   high evaporation rate which tends to further suppress the surface heating.

348   In Fig. 8b the dimensionless droplet mass and droplet volume (solid and dashed lines,

349   respectively) are shown for the cases (We,T_∞)=(15, 600) and (15, 1000). Up to the breakup

350   instant, the evaporated mass is less than 0.5%, while the droplet volume increases up to 0.1%

351   due to the thermal expansion effect. Note that in the corresponding cases with n-heptane

352   presented in [61], the maximum heat-up was 7K, the evaporated mass was reaching 2% and

353   the thermal expansion effect was absent. The aforementioned differences are mainly affected

354   by the different volatility between the n-heptane and n-decane.

355

356
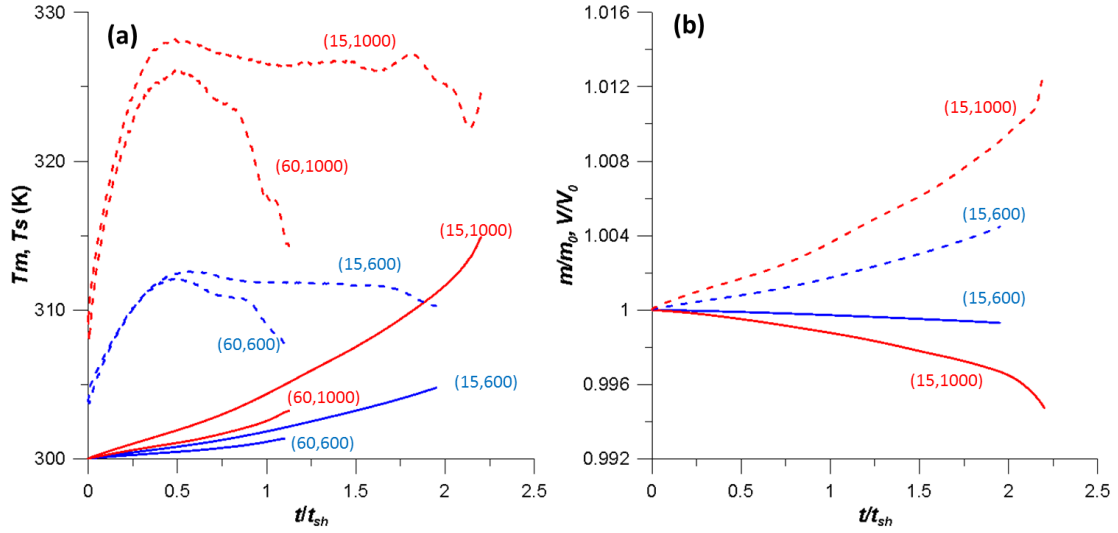
Fig. 8: (a) Temporal evolution of mean droplet temperature T_m (solid lines) and spatially averaged surface temperature T_s (dashed lines). In (b) temporal evolution of dimensionless droplet mass (solid lines) and dimensionless droplet volume (dashed lines). The cases shown in parentheses correspond to (We, T_∞).

361

The heat and mass transfer processes are usually characterized by the dimensionless Nusselt (Nu) and Sherwood (Sh) numbers respectively, which express the heat/mass transfer enhancement relative to a purely diffusive process. These are defined as the dimensionless temperature/concentration gradient at the droplet interface, but their calculation is not applicable with the VOF methodology due to the continuous variation of the field magnitudes across the interface as explained in [60]. Inspired by Hase and Weigand [58] an indirect method is used to estimate them, through the Eqs. 10-12:

$$\rho_l V \frac{d(c_{p,l}T_m)}{dt} = S\left(\frac{Nu \cdot k_{g,\infty}}{D_0}(T_\infty - T_s) - \dot{m}''L\right) \tag{10}$$

$$\dot{m} = S\frac{Sh \cdot \rho_{g,\infty}D_{AB,\infty}}{D_0}ln(1 + B_M) \tag{11}$$

19

$$Nu_l \cdot k_{l,0} \frac{T_s - T_m}{D_0} = Nu \cdot k_{g,\infty} \frac{T_\infty - T_s}{D_0} - \dot{m}'' L \tag{12}$$

369

370   Eq. 10 is the droplet energy balance, Eq. 11 is a widely used relationship for the evaporation

371   rate of spherical droplets and Eq. 12 represents the heat flux continuity at the droplet's

372   surface, in which Nu_l is the dimensionless temperature gradient inside the liquid; this equation

373   connects the average droplet temperature T_m with the surface temperature T_s. The set of Eqs.

374   10-12 also forms a variant of the 0-D model for spherical droplet evaporation proposed by

375   Renksizbulut et al. [75]. Solving Eqs. 10-12 for Nu, Sh and Nu_{liq} and using the CFD data for

376   the mean droplet temperature T_m, the space averaged surface temperature T_s and the

377   evaporation rate dm/dt, the temporal variation of the dimensionless transfer numbers is

378   obtained; this is shown in Fig. 9 for the case $(We,T_\infty)=(15, 600)$, which can be regarded as

379   representative, since the qualitative behavior observed is similar in all cases examined. For

380   the Nu and Sh numbers, there is a short initial transitional period as the one observed in [39,

381   40, 58]; after that, they exhibit small fluctuations in time. The Sh number seems to oscillate

382   around a steady-state value, while the Nu number decreases continuously in time with a slow

383   rate. On the other hand, the Nu_{liq} number exhibits a more unsteady behavior. The initial

384   transitional period is longer compared to the other numbers and its magnitude exhibits almost

385   one order of magnitude larger variations with time.

386
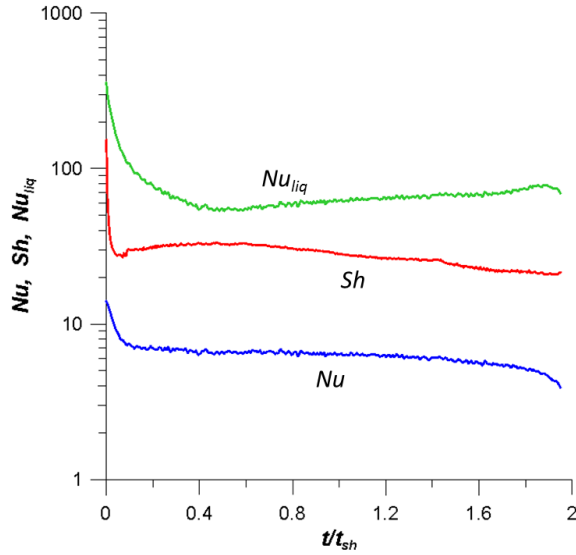
Fig. 9: Temporal variation of Nu, Sh and Nu_l for the case of $(We,T_\infty)=(15,600)$.

It is of engineering interest to find expressions for the Nu, Sh and Nu_{liq} numbers and use them in 0-D or 1-D models aiming to predict the droplet temperature and the evaporation rate. Earlier CFD works on spherical droplets (see [39, 40] among many others) provided such expressions as a function of the instantaneous Re, B_T and B_M numbers. Nevertheless, this is not applicable in the case of droplet breakup due to the short duration of the phenomenon and more importantly due to shape distortion from the spherical one. In [61] time-averaged transfer numbers (being a function of the initial reference conditions) were used and they could adequately capture the thermal behavior of droplets undergoing breakup. Following this approach, the time-averaged transfer numbers fitting the present data are given in Eqs. 13-15; the Re_l appearing in Eq. 15 ($Re_l = Re_\infty \varepsilon^{2/3} N^{-4/3}$) was taken from [38] and it is derived by equating the tangential shear stresses at the droplet surface:

$$\overline{Nu} = \frac{2 + 6.83 Re_\infty^{0.07} Pr_{g,\infty}^{1/3}}{\left(1 + B_{T,\infty}\right)^{0.75}} \tag{13}$$

21

$$\overline{Sh} = \left(2 + 1.608 We_0^{0.591} Sc_{g,\infty}^{1/3}\right)\left(1 + B_{T,\infty}\right) \tag{14}$$

$$\overline{Nu_l} = 55.95 + Re_l Pr_l^{1.6}/1429 \tag{15}$$

402

403   The set of Eqs. 10-15 forms a 0-D model which can be used to predict the average droplet

404   heating and evaporation, but not the transient variation of the surface temperature, which

405   decreases after reaching a maximum (see Fig. 8a). The reason for that discrepancy is that the

406   time-averaged expressions ignore the transient behavior of the transfer numbers. In the

407   present work, the Nu and Nu_{liq} numbers are expressed as a function of the non-dimensional

408   time and this is an improvement of the model used in [61]; the correlations used are shown in

409   Table 1 and they are valid for the conditions examined in the present work.

410

411   Table 1: Transient Nu and Nu_{liq} numbers. The time t corresponds to the dimensionless time

412   t/t_{sh}.

	$Nu = c_0 - c_1 t + c_2 \exp(-c_3 t)$	$Nu_l = c_0 + c_1 \exp(-c_2 t) + c_3 \cos(2\pi t/c_4)$
c_0	$1.326 Re_\infty^{0.3647}\left(1 + B_{T,\infty}\right)^{-0.236}$	$56.47 + 7.65 \cdot 10^{-4} Re_l^{1.707}\left(1 + B_{T,\infty}\right)^{-0.432}$
c_1	$3 \cdot 10^{-6} Re_\infty^{2.212}\left(1 + B_{T,\infty}\right)^{2.226}$	$201 + 1.99 \cdot 10^{-4} Re_l^{2.25}\left(1 + B_{T,\infty}\right)^{-0.5285}$
c_2	3	$15.59 + 1.65 \cdot 10^{-6} Re_l^{2.64}\left(1 + B_{T,\infty}\right)^{-0.623}$
c_3	60	$5.786 \cdot 10^{-5} Re_l^{2.226}\left(1 + B_{T,\infty}\right)^{-0.825}$
c_4	$-$	1.2

413

22

414   The results of the 0-D model by using the transient correlations for Nu and Nu_{liq} are shown in

415   Fig. 10 for the case of We=45 and three different gas phase temperatures; the solid and the

416   dashed lines correspond to the CFD and the 0-D model predictions, respectively. As seen, the

417   time dependent expressions for the transfer number can adequately predict the transient

418   behavior of the surface temperature, with a less than 4K error. The model predictions

419   presented in Fig. 10 have assumed that the temporal evolution of the surface area is known

420   and this is a limitation of the proposed model. On the other hand, the Eq. 8 for the surface

421   area evolution can be used to predict the thermal behavior for $t<t_{sh}$; in this case, the errors are

422   mainly determined by the effectiveness of the curve reproducing the surface area evolution.

423
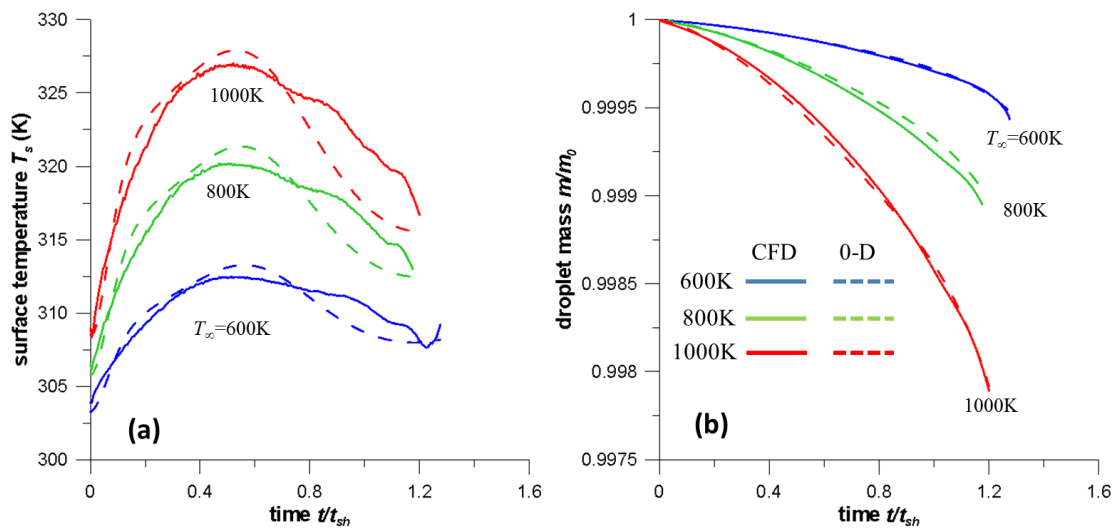
424

425   Fig. 10: Predictions of the 0-D model for (a) the spatially averaged surface temperature and

426   (b) the droplet mass for the case of We=45. The solid lines are the CFD data and the dashed

427   lines are the 0-D model predictions.

428

429   In Strotos et al. [61] it was shown that droplet breakup is affected by heating when the We

430   number is low and the ambient temperature is high. This conclusion was drawn both by

431　considering the associated timescales (either in a macroscopic or a microscopic level) and by

432　implementing the aforementioned 0-D model with the time-averaged expressions for the

433　transfer numbers. These comments are also verified by the present simulations for an n-

434　decane droplet. Relating the n-heptane CFD simulations performed in [61] and the present

435　ones for the n-decane, the surface temperature at $t=t_{sh}$ is well represented by Eq. 16. This

436　equation clearly demonstrates the effect of We number, gas phase temperature and species

437　volatility through the heating factor F_{heat}:

438

$$T_s(t_{sh}) = T_0\big(1 + 0.0195 We^{-0.2532} F_{heat}^{2.053}\big) \tag{16}$$

439

440　## 3.4　Spatial distribution of the flow variables

441　The spatial distribution of surface temperature, inner droplet temperature and vapor

442　concentration field are shown in Fig. 11 and Fig. 12 for the cases with $T_\infty=800K$ and We

443　number 15 and 30, respectively. The surface temperature (denoted with a thick line colored

444　with the corresponding temperature values) is not spatially uniform; along the droplet surface

445　differences of 15K can be observed. In the initial flattening phase, hot spots are observed on

446　the front side of the droplet in an off-axis location; at subsequent instances hot spots are

447　observed at the rear of the droplet. In a spherical droplet case these temperature differences

448　along the surface could induce secondary flow (due to surface tension gradients) and form

449　cellular vortices. The present work has included the effect of surface tension variation along

450　the interface through the CSS surface tension model [76]. Nevertheless, no secondary flow

451　was observed in the present cases (see characteristic streamlines in the left column), since the

452　flow patterns are determined by the droplet shape. Regarding the inner temperature field and

453   the vapor concentration field in the gas phase, these follow similar patterns to the ones

454   observed in [61], as affected by the local velocity field and the droplet deformation.

455
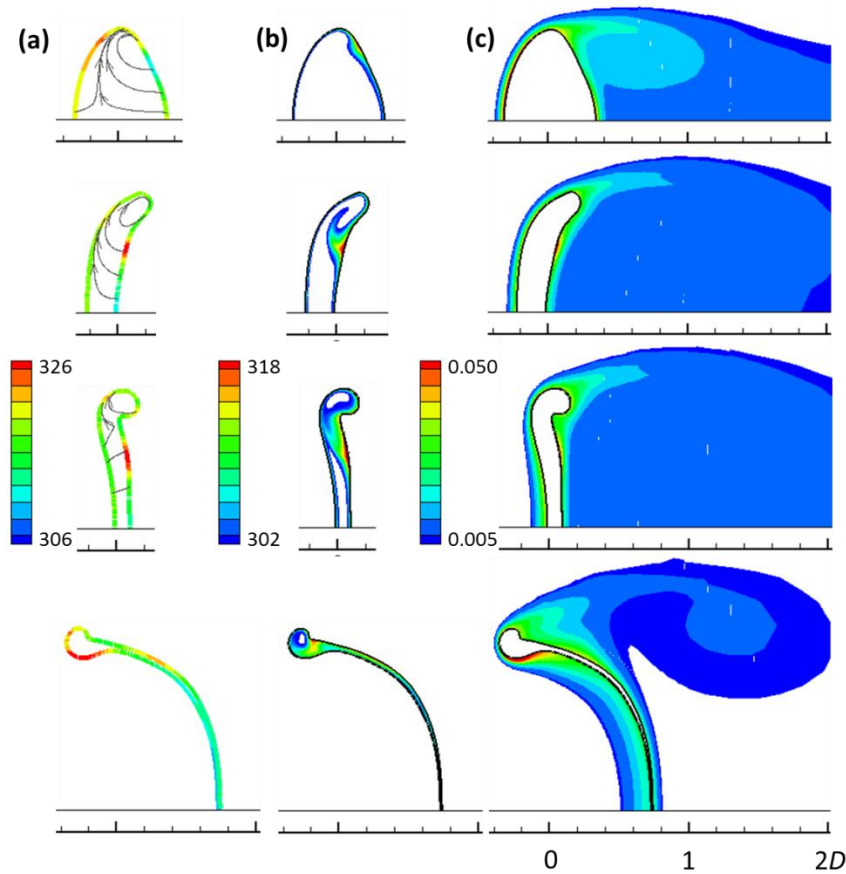
456

457   Fig. 11: Spatial distribution of (a) surface temperature, (b) droplet temperature and (c) vapor

458   concentration for the case (We, T_∞)= (15, 800). The time instances presented are 0.5, 1.0, 1.5

459   and 2.0t_{sh}. In (a) characteristic streamlines are also shown. For color interpretation, see the

460   online version.

461
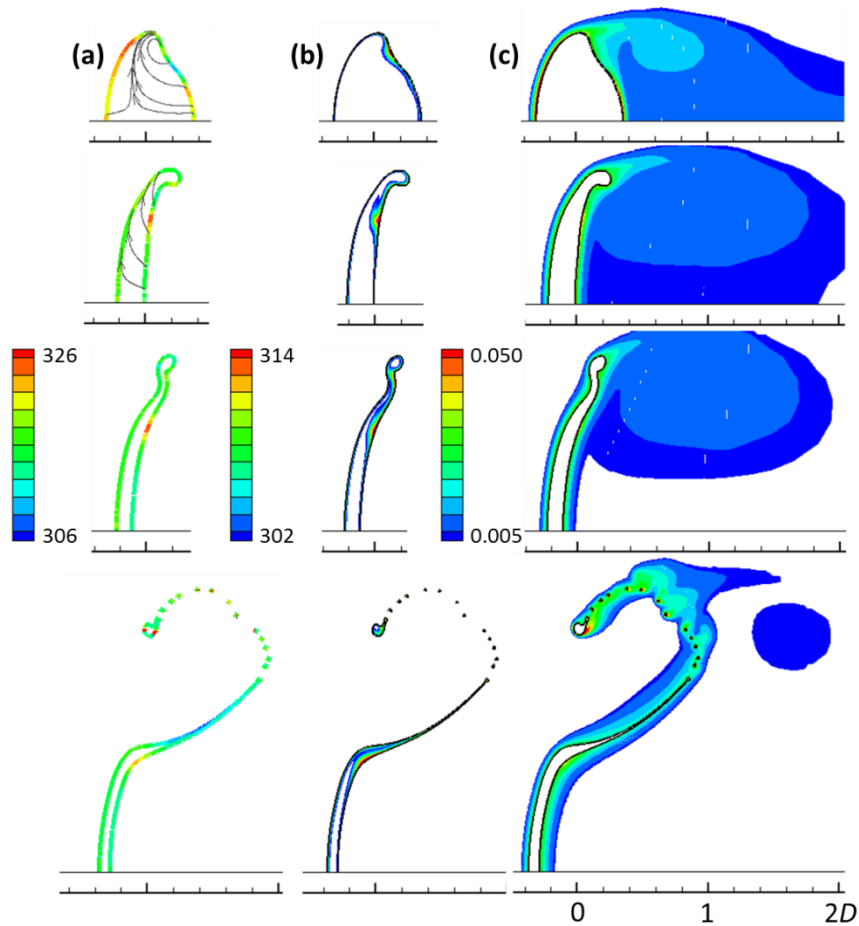
Fig. 12: Spatial distribution of (a) surface temperature, (b) droplet temperature and (c) vapor concentration for the case (We, T_∞)= (30, 800). The time instances presented are 0.5, 1.0, 1.25 and 1.5t_{sh}. In (a) characteristic streamlines are also shown. For color interpretation, see the online version.

4 Conclusions

The Navier-Stokes, energy and transport of species conservation equations together with the VOF methodology have been utilized to study the coupled problem of aerodynamic droplet breakup under the influence of heating and evaporation for We numbers in the range 15-90 and gas phase temperatures 600-1000K. To quantify the effect of heating, the same cases

26

473   were also studied under isothermal conditions assuming constant species properties.

474   Combining the results obtained from the present work for an n-decane fuel droplet with those

475   for a more volatile n-heptane droplet presented in Strotos et al. [61], it seems that droplet

476   heating affects the overall breakup performance for low *We* numbers, high gas phase

477   temperatures and low volatility fuels. For a non-breaking-up case with constant properties,

478   heating may decrease the surface tension coefficient in such a way, that droplet not only

479   breaks up in the bag breakup regime, but also in the transitional breakup regime.

480   Nevertheless, at high *We* numbers the surface tension still decreases but without altering the

481   breakup performance. During droplet breakup, despite the fact that the liquid evaporated mass

482   is very low (especially for low volatility fuels), one has to consider the evaporation source

483   terms since they play an important role by suppressing the droplet heat-up; this is evident for

484   high volatility fuels which seem to be less affected by heating.

485   The concept of "heating factor" was introduced which provides an indication of the droplet

486   tendency to heat-up by combining the terms tending to increase and decrease the droplet

487   temperature. Useful correlations were provided for an a-priori estimation of the breakup

488   instant, surface area evolution and droplet heat-up. Additional to them, an enhanced 0-D

489   model able to predict the thermal behavior of the droplet is proposed. In relevance to our

490   previous work [61], it uses time-dependent transfer numbers instead of time-averaged and it is

491   able to capture the transient behavior of the spatially average surface temperature. The latter

492   is not spatially uniform and peak values are observed in the front of the droplet in the initial

493   flattening phase and at the rear of the droplet in the subsequent stages.

494

5 Acknowledgements

6 Nomenclature

Roman symbols

Symbol	Description	Units
B_M	Mass transfer Spalding number	-
B_T	Heat transfer Spalding number	-
c_p	Heat capacity	J/kgK
D	diameter	m
D_{AB}	Vapor diffusion coefficient	m^2/s
F_{heat}	heating factor	-
Oh	Ohnesorge number $Oh = \mu_l / \sqrt{\rho_l \sigma D_0}$	-
k	Thermal conductivity	W/mK
L	Latent heat of vaporization	J/kg
m	mass	kg
$\dot{m}''$	Evaporation rate per unit area	kg/m^2s
Nu	Nusselt number	-
Pr	Prandtl number	-
R	radius	m
Re	Reynolds number $Re = \rho_g U_{rel,0} D_0 / \mu_g$	-
S	surface area	m^2
Sc	Schmidt number	-
Sh	Sherwood number	-
t	time	s
t_{sh}	Shear breakup timescale $t_{sh} = D\sqrt{\varepsilon}/U$	-
T	temperature	K
U	reference velocity	m/s
u	instantaneous droplet velocity	m/s
V	volume	m^3
We	Weber number $We = \rho_g U_{rel,0}^2 D_0 / \sigma$	-
We_t	instantaneous We number	-
Y	vapor concentration	kg/kg

Greek symbols

Symbol	Description	Units
a	thermal diffusivity	m^2/s
γ	thermal effusivity $\gamma = \sqrt{k\rho c_p}$	J/m^2K$s^{0.5}$

28

ε	density ratio $\varepsilon = \rho_l/\rho_g$		-
μ	viscosity		kg/ms
N	viscosity ratio $N = \mu_l/\mu_g$		-
v	kinematic viscosity		m^2/s
ρ	density		kg/m^3
σ	surface tension coefficient		N/m

505

Subscripts

Symbol	Description
0	initial
c	cross-stream
cr	critical
g	gas
l	liquid
rel	relative
s	at surface
t	instantaneous magnitude
x,y,z	coordinates
∞	free-stream conditions

506

Abbreviations

Symbol	Description
C07	n-heptane C_7H_{16}
C10	n-decane $C_{10}H_{22}$
CFD	Computational Fluid Dynamics
cpR	Cells per Radius
CSS	Continuum Surface Stress
UDF	User Defined Function
VOF	Volume of Fluid

507

508 # References
509

510 [1] D.R. Guildenbecher, C. López-Rivera, P.E. Sojka, Secondary atomization, Experiments in
511 Fluids, 46 (2009) 371-402.

512 [2] M. Pilch, C. Erdman, Use of breakup time data and velocity history data to predict the
513 maximum size of stable fragments for acceleration-induced breakup of a liquid drop,
514 International Journal of Multiphase Flow, 13 (1987) 741-757.

515 [3] G.M. Faeth, L.P. Hsiang, P.K. Wu, Structure and breakup properties of sprays,
516 International Journal of Multiphase Flow, 21, Supplement (1995) 99-127.

29

517   [4] B.E. Gelfand, Droplet breakup phenomena in flows with velocity lag, Progress in Energy
518   and Combustion Science, 22 (1996) 201-265.

519   [5] T.G. Theofanous, Aerobreakup of Newtonian and Viscoelastic Liquids, Annual Review of
520   Fluid Mechanics, 43 (2011) 661-690.

521   [6] J.A. Nicholls, A.A. Ranger, Aerodynamic shattering of liquid drops, AIAA Journal, 7
522   (1969) 285-290.

523   [7] S.A. Krzeczkowski, Measurement of liquid droplet disintegration mechanisms,
524   International Journal of Multiphase Flow, 6 (1980) 227-239.

525   [8] L.P. Hsiang, G.M. Faeth, Near-limit drop deformation and secondary breakup,
526   International Journal of Multiphase Flow, 18 (1992) 635-652.

527   [9] L.P. Hsiang, G.M. Faeth, Drop properties after secondary breakup, International Journal
528   of Multiphase Flow, 19 (1993) 721-735.

529   [10] L.P. Hsiang, G.M. Faeth, Drop deformation and breakup due to shock wave and steady
530   disturbances, International Journal of Multiphase Flow, 21 (1995) 545-560.

531   [11] W.H. Chou, L.P. Hsiang, G.M. Faeth, Temporal properties of drop breakup in the shear
532   breakup regime, International Journal of Multiphase Flow, 23 (1997) 651-669.

533   [12] W.H. Chou, G.M. Faeth, Temporal properties of secondary drop breakup in the bag
534   breakup regime, International Journal of Multiphase Flow, 24 (1998) 889-912.

535   [13] Z. Dai, G.M. Faeth, Temporal properties of secondary drop breakup in the multimode
536   breakup regime, International Journal of Multiphase Flow, 27 (2001) 217-236.

537   [14] Z. Liu, R.D. Reitz, An analysis of the distortion and breakup mechanisms of high speed
538   liquid drops, International Journal of Multiphase Flow, 23 (1997) 631-650.

539   [15] C.H. Lee, R.D. Reitz, An experimental study of the effect of gas density on the distortion
540   and breakup mechanism of drops in high speed gas stream, International Journal of
541   Multiphase Flow, 26 (2000) 229-244.

542   [16] X.-K. Cao, Z.-G. Sun, W.-F. Li, H.-F. Liu, Z.-H. Yu, A new breakup regime of liquid
543   drops identified in a continuous and uniform air jet flow, Physics of Fluids, 19 (2007)
544   057103.

545   [17] H. Zhao, H.-F. Liu, W.-F. Li, J.-L. Xu, Morphological classification of low viscosity

546   drop bag breakup in a continuous air jet stream, Physics of Fluids, 22 (2010) 114103.

547   [18] H. Zhao, H.-F. Liu, J.-L. Xu, W.-F. Li, K.-F. Lin, Temporal properties of secondary drop

548   breakup in the bag-stamen breakup regime, Physics of Fluids, 25 (2013) 054102.

549   [19] L. Opfer, I.V. Roisman, C. Tropea, Aerodynamic Fragmentation of Drops: Dynamics of

550   the Liquid Bag, in: ICLASS 2012, Heidelberg, Germany, 2012.

551   [20] L. Opfer, I.V. Roisman, J. Venzmer, M. Klostermann, C. Tropea, Droplet-air collision

552   dynamics: Evolution of the film thickness, Physical Review E, 89 (2014) 013023.

553   [21] D.R. Guildenbecher, P.E. Sojka, Experimental investigation of aerodynamic

554   fragmentation of liquid drops modified by electrostatic surface charge, Atomization and

555   Sprays, 21 (2011) 139-147.

556   [22] A.K. Flock, D.R. Guildenbecher, J. Chen, P.E. Sojka, H.J. Bauer, Experimental statistics

557   of droplet trajectory and air flow during aerodynamic fragmentation of liquid drops,

558   International Journal of Multiphase Flow, 47 (2012) 37-49.

559   [23] J. Han, G. Tryggvason, Secondary breakup of axisymmetric liquid drops. II. Impulsive

560   acceleration, Physics of Fluids, 13 (2001) 1554-1565.

561   [24] C. Aalburg, Deformation and breakup of round drop and nonturbulent liquid jets in

562   uniform crossflows, in: Aerospace Engineering and Scientic Computing, University of

563   Michigan, 2002.

564   [25] S. Khosla, C.E. Smith, Detailed Understanding of Drop Atomization by Gas Crossflow

565   Using the Volume of Fluid Method, in: ILASS Americas, Toronto, Canada, 2006.

566   [26] S. Quan, D.P. Schmidt, Direct numerical study of a liquid droplet impulsively

567   accelerated by gaseous flow, Physics of Fluids, 18 (2006) 103103.

568   [27] A.R. Wadhwa, V. Magi, J. Abraham, Transient deformation and drag of decelerating

569   drops in axisymmetric flows, Physics of Fluids, 19 (2007) 113301.

570   [28] F. Xiao, M. Dianat, J.J. McGuirk, LES of Single Droplet and Liquid Jet Primary Break-

571   up Using a Coupled Level Set/Volume of Fluid Method, in: 12th ICLASS, Heidelberg,

572   Germany, 2012.

573 [29] P. Khare, V. Yang, Drag Coefficients of Deforming and Fragmenting Liquid Droplets,
574 in: ILASS Americas, 2013.

575 [30] M. Jalaal, K. Mehravaran, Transient growth of droplet instabilities in a stream, Physics
576 of Fluids, 26 (2014) 012101.

577 [31] M. Jain, R.S. Prakash, G. Tomar, R.V. Ravikrishna, Secondary breakup of a drop at
578 moderate Weber numbers, Proceedings of the Royal Society of London A: Mathematical,
579 Physical and Engineering Sciences, 471 (2015).

580 [32] W. Yang, M. Jia, K. Sun, T. Wang, Influence of density ratio on the secondary
581 atomization of liquid droplets under highly unstable conditions, Fuel, 174 (2016) 25-35.

582 [33] G. Strotos, I. Malgarinos, N. Nikolopoulos, M. Gavaises, Predicting droplet deformation
583 and breakup for moderate Weber numbers, International Journal of Multiphase Flow, 85
584 (2016) 96–109.

585 [34] S.D. Givler, J. Abraham, Supercritical droplet vaporization and combustion studies,
586 Progress in Energy and Combustion Science, 22 (1996) 1-28.

587 [35] J. Bellan, Supercritical (and subcritical) fluid behavior and modeling: drops, streams,
588 shear and mixing layers, jets and sprays, Progress in Energy and Combustion Science, 26
589 (2000) 329-366.

590 [36] S.S. Sazhin, Advanced models of fuel droplet heating and evaporation, Progress in
591 Energy and Combustion Science, 32 (2006) 162-214.

592 [37] H.Y. Erbil, Evaporation of pure liquid sessile and spherical suspended drops: A review,
593 Advances in Colloid and Interface Science, 170 (2012) 67-86.

594 [38] M. Renksizbulut, R.J. Haywood, Transient droplet evaporation with variable properties
595 and internal circulation at intermediate Reynolds numbers, International Journal of
596 Multiphase Flow, 14 (1988) 189-202.

597 [39] R.J. Haywood, R. Nafziger, M. Renksizbulut, Detailed examination of gas and liquid
598 phase transient processes in convective droplet evaporation, Journal of Heat Transfer, 111
599 (1989) 495-502.

600 [40] C.H. Chiang, M.S. Raju, W.A. Sirignano, Numerical analysis of convecting, vaporizing
601 fuel droplet with variable properties, International Journal of Heat and Mass Transfer, 35
602 (1992) 1307-1324.

603 [41] C.M. Megaridis, Comparison between experimental measurements and numerical
604 predictions of internal temperature distributions of a droplet vaporizing under high-
605 temperature convective conditions, Combustion and Flame, 93 (1993) 287-302.

606 [42] A.T. Shih, C.M. Megaridis, Suspended droplet evaporation modeling in a laminar
607 convective environment, Combustion and Flame, 102 (1995) 256-270.

608 [43] A.T. Shih, C.M. Megaridis, Thermocapillary flow effects on convective droplet
609 evaporation, International Journal of Heat and Mass Transfer, 39 (1996) 247-257.

610 [44] M.M. Abou Al-Sood, M. Birouk, A numerical study of the effect of turbulence on mass
611 transfer from a single fuel droplet evaporating in a hot convective flow, International Journal
612 of Thermal Sciences, 46 (2007) 779-789.

613 [45] S. Raghuram, V. Raghavan, D.N. Pope, G. Gogos, Two-phase modeling of evaporation
614 characteristics of blended methanol–ethanol droplets, International Journal of Multiphase
615 Flow, 52 (2013) 46-59.

616 [46] J. Schlottke, B. Weigand, Direct numerical simulation of evaporating droplets, Journal of
617 Computational Physics, 227 (2008) 5215-5237.

618 [47] N. Ghata, B.D. Shaw, Computational modeling of the effects of support fibers on
619 evaporation of fiber-supported droplets in reduced gravity, International Journal of Heat and
620 Mass Transfer, 77 (2014) 22-36.

621 [48] C.M. Megaridis, W.A. Sirignano, Numerical modeling of a vaporizing multicomponent
622 droplet, Symposium (International) on Combustion, 23 (1990) 1413-1421.

623 [49] C.M. Megaridis, W.A. Sirignano, Multicomponent droplet vaporization in a laminar
624 convective environment, Combustion science and technology, 87 (1992) 27-44.

625 [50] C.M. Megaridis, Liquid-Phase Variable Property Effects in Multicomponent Droplet
626 Convective Evaporation, Combustion Science and Technology, 92 (1993) 291 - 311.

627 [51] M. Renksizbulut, M. Bussmann, Multicomponent droplet evaporation at intermediate
628 Reynolds numbers, International Journal of Heat and Mass Transfer, 36 (1993) 2827-2835.

629 [52] G. Strotos, M. Gavaises, A. Theodorakakos, G. Bergeles, Numerical investigation of the
630 evaporation of two-component droplets, Fuel, 90 (2011) 1492-1507.

631 [53] R. Banerjee, Numerical investigation of evaporation of a single ethanol/iso-octane
632 droplet, Fuel, 107 (2013) 724-739.

633 [54] G. Strotos, I. Malgarinos, N. Nikolopoulos, M. Gavaises, Predicting the evaporation rate
634 of stationary droplets with the VOF methodology for a wide range of ambient temperature
635 conditions, International Journal of Thermal Sciences, 109 (2016) 253–262.

636 [55] R.J. Haywood, M. Renksizbulut, G.D. Raithby, Numerical solution of deforming
637 evaporating droplets at intermediate Reynolds numbers, Numerical Heat Transfer; Part A:
638 Applications, 26 (1994) 253-272.

639 [56] R.J. Haywood, M. Renksizbulut, G.D. Raithby, Transient deformation and evaporation
640 of droplets at intermediate Reynolds numbers, International Journal of Heat and Mass
641 Transfer, 37 (1994) 1401-1409.

642 [57] Z.S. Mao, T. Li, J. Chen, Numerical simulation of steady and transient mass transfer to a
643 single drop dominated by external resistance, International Journal of Heat and Mass
644 Transfer, 44 (2001) 1235-1247.

645 [58] M. Hase, B. Weigand, Transient heat transfer of deforming droplets at high Reynolds
646 numbers, International Journal of Numerical Methods for Heat & Fluid Flow, 14 (2003) 85 -
647 97.

648 [59] J. Schlottke, E. Dulger, B. Weigand, A VOF-based 3D numerical investigation of
649 evaporating, deformed droplets, Progress in Computational Fluid Dynamics, an International
650 Journal, 9 (2009) 426-435.

651 [60] R.F.L. Cerqueira, E.E. Paladino, C.R. Maliska, A computational study of the interfacial
652 heat or mass transfer in spherical and deformed fluid particles flowing at moderate Re
653 numbers, Chemical Engineering Science, 138 (2015) 741-759.

654   [61] G. Strotos, I. Malgarinos, N. Nikolopoulos, M. Gavaises, Numerical investigation of

655   aerodynamic droplet breakup in a high temperature gas environment, Fuel, 181 (2016) 450-

656   462.

657   [62] A. Theodorakakos, G. Bergeles, Simulation of sharp gas–liquid interface using VOF

658   method and adaptive grid local refinement around the interface, International Journal for

659   Numerical Methods in Fluids, 45 (2004) 421-439.

660   [63] I. Malgarinos, N. Nikolopoulos, M. Marengo, C. Antonini, M. Gavaises, VOF

661   simulations of the contact angle dynamics during the drop spreading: Standard models and a

662   new wetting force model, Advances in Colloid and Interface Science, 212 (2014) 1-20.

663   [64] R.H. Perry, D.W. Green, Perry's Chemical Engineers' Handbook, 7th ed., McGraw-Hill,

664   1997.

665   [65] B.E. Poling, J.M. Prausnitz, J.P. O'Connell, Properties of Gases and Liquids (5th

666   Edition), in, McGraw-Hill, 2001.

667   [66] ANSYS®FLUENT, Release 14.5, Theory Guide, in, 2012.

668   [67] I. Malgarinos, N. Nikolopoulos, M. Gavaises, Coupling a local adaptive grid refinement

669   technique with an interface sharpening scheme for the simulation of two-phase flow and free-

670   surface flows using VOF methodology, Journal of Computational Physics, 300 (2015) 732-

671   753.

672   [68] G. Strotos, I. Malgarinos, N. Nikolopoulos, K. Papadopoulos, A. Theodorakakos, M.

673   Gavaises, Performance of VOF methodology in predicting the deformation and breakup of

674   impulsively accelerated droplets in: 13th ICLASS, Tainan, Taiwan, 2015.

675   [69] R. Clift, J.R. Grace, M.E. Weber, Bubbles, drops and particles, Academic Press, New

676   York, 1978.

677   [70] E.E. Michaelides, Particles, bubbles & drops: their motion, heat and mass transfer, World

678   Scientific, 2006.

679   [71] F.P. Incropera, D.P. de Witt, Fundamentals of Heat and Mass Transfer 3rd ed., Wiley,

680   New York, 1990.

681 [72] M. Seki, H. Kawamura, K. Sanokawa, Transient temperature profile of a hot wall due to
682 an impinging liquid droplet, Journal of Heat Transfer, 100 (1978) 167-169.

683 [73] G. Strotos, G. Aleksis, M. Gavaises, K.-S. Nikas, N. Nikolopoulos, A. Theodorakakos,
684 Non-dimensionalisation parameters for predicting the cooling effectiveness of droplets
685 impinging on moderate temperature solid surfaces, International Journal of Thermal Sciences,
686 50 (2011) 698-711.

687 [74] G. Strotos, N. Nikolopoulos, K.-S. Nikas, K. Moustris, Cooling effectiveness of droplets
688 at low Weber numbers: Effect of temperature, International Journal of Thermal Sciences, 72
689 (2013) 60-72.

690 [75] M. Renksizbulut, M. Bussmann, X. Li, Droplet vaporization model for spray
691 calculations, Particle & Particle Systems Characterization, 9 (1992) 59-65.

692 [76] B. Lafaurie, C. Nardone, R. Scardovelli, S. Zaleski, G. Zanetti, Modelling Merging and
693 Fragmentation in Multiphase Flows with SURFER, Journal of Computational Physics, 113
694 (1994) 134-147.

695

696